JOURNAL OF SPACECRAFT AND ROCKETS
Vol. 43, No. 1, January–February 2006

Vibration Isolator for Large Space Telescopes

Allen J. Bronowicki*
Northrop Grumman Space Technology, Redondo Beach, California 90278

A full spacecraft vibration isolator for the James Webb Space Telescope is described. This 1-Hz isolator brings wavefront errors and line-of-sight pointing jitter induced by reaction wheel and cryocooler compressor disturbances down to below a few nanometers and milliarcseconds, respectively. The isolator consists of four passively damped beams connecting the corners of the spacecraft to a thermal isolation tower positioning the telescope. An efficient analysis approach was developed based upon a fractional derivative model of the viscoelastic material. The technique employs modal data from a finite element model for a constant operating temperature and frequency. The modal properties are adjusted using frequency- and temperature-dependent properties from the viscoelastic material's constitutive model. Development test results for the unit isolator elements are presented and compared to model predictions. Results of a dynamic test on an assembled isolator are also presented. The test employs a simulator replicating the full mass and inertia of the telescope. A series of modal surveys was performed across the operating temperature range to validate model predictions.

Nomenclature

a, b = zero and pole of fractional derivative viscoelastic material model
E = axial modulus
$\boldsymbol{F}$ = force vector
f = operating frequency, Hz
f_R = reduced frequency
G^*, G' = complex shear modulus
$\boldsymbol{h}$ = modal response amplitude vector
I = bending moment of inertia of isolator tube
K_E = elastic portion of system stiffness matrix
K_V = lossy portion of system stiffness matrix
$K4$ = system structural damping matrix
k_C = constraining layer axial stiffness per unit circumference
k_S = lateral stiffness of an individual isolator strut
k_V = damping layer shear stiffness per unit circumference
k_W = tube wall axial stiffness per unit circumference
$k_{X,Y,Z}$ = X, Y, and Z global stiffnesses of isolator assembly
L = free length of isolator strut
L_c = constraining layer segment length
M = system mass matrix
m_B = mass of bus
m_R = reduced mass of bus-telescope two-body system
m_T = mass of telescope
S^V = dynamic stiffness scaling function
T = absolute operating temperature, K
t = layer thickness
$\boldsymbol{u}$ = physical response amplitude vector
α = temperature shift function
β = exponent (slope) of fractional derivative VEM model
η = loss factor
η^V = loss factor scaling function
$\kappa 4$ = system structural damping matrix in modal space
λ = decay length between constraint and base tube
$\boldsymbol{\Phi}$ = matrix of mode shape vectors
Ω = operating frequency, radians/s
ω = diagonal matrix of natural frequencies of vibration

I. Introduction

THE James Webb Space Telescope (JWST) design incorporates a 6.5-m aperture, 18-segment primary mirror (PM), as well as a deployable secondary mirror (SM).[1] Six of the PM segments are mounted on two deployable wings, the remainder being on a fixed center section. The entire optical payload is then positioned on a deployable tower to separate it thermally from the equipment module or spacecraft bus. A five-layer sunshield placed on top of the bus provides passive cooling of the payload to about 40 K. The thermal isolation tower is connected to the corners of the bus with a set of four axially flexured, passively damped beams. This simple arrangement provides vibration isolation to the payload, as will be described in this paper. The deployed observatory we currently envision is shown in Fig. 1.

Because of the large aperture, along with volume and weight limitations in the launch vehicle and the requirement for deployment, the JWST structural system is of necessity much more flexible than prior space telescopes.[2] For instance, the current JWST design has a 7-Hz SM support structure lateral mode and a 13-Hz PM twist mode. On the Hubble Space Telescope (HST), comparable modes are at 34 and 50 Hz for the SM and PM, respectively.[3]

The inherent structural damping in this precision cryogenic structure can be no greater than 0.1% of critical, typical for optical support structures, and potentially much lower because of the reduction in material damping with cold. One study on monolithic graphite/epoxy coupons suspended in a cryovacuum chamber has shown that damping below 50 K averages about one-fourth of its room-temperature value, with viscous damping ratios as low as 0.005% having been observed.[4] Damping the JWST telescope structure is a difficult proposition. Passive viscoelastic materials and viscous fluid dampers would freeze. Active damping loops would need to be tuned in cryogenic conditions and would need to emit almost no power to avoid heating the structure. The most promising approach for vibration absorption is the use of eddy current tuned mass dampers in targeted locations.[5] Magnetic dampers are under consideration to add margin to the vibration mitigation system, but are not a requirement because of the large amount of isolation provided by the design described in this paper.

For this class of space telescope, attitude control is effected by torquing against reaction wheels, whose speeds are allowed to run up and down within spin rate limits. The main source of angular momentum accumulation is solar pressure on the large deployed sunshield, because the center of pressure cannot be aligned with the center of gravity for all observatory pointing orientations. As wheels approach speed limits, thrusters are fired to remove angular momentum from the observatory, and the wheels are spun back down. Constant spinning of the wheels produces vibratory disturbances

---

Presented as Paper 2004-1903 at the Structures, Structural Dynamics, and Materials Conference, Palm Springs, CA, 19–22 April 2004; received 16 July 2004; revision received 27 January 2005; accepted for publication 25 February 2005. Copyright © 2005 by the American Institute of Aeronautics and Astronautics, Inc. All rights reserved. Copies of this paper may be made for personal or internal use, on condition that the copier pay the $10.00 per-copy fee to the Copyright Clearance Center, Inc., 222 Rosewood Drive, Danvers, MA 01923; include the code 0022-4650/06 $10.00 in correspondence with the CCC.

*Technical Fellow, R8/2874, Integrated Modeling, One Space Park Drive.

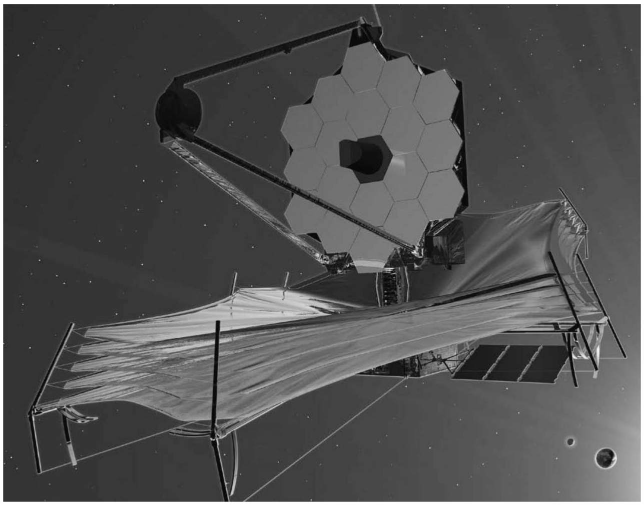

Fig. 1 Artist rendition of the deployed James Webb Space Telescope.

because of imbalance and bearing imperfections. Disturbances at harmonics of the wheel speed can coincide with any number of payload resonances and dwell for a long time. Given that the reaction wheels for HST and JWST have roughly similar disturbance levels,[6,7] its greater flexibility and lower damping dictate a more comprehensive vibration mitigation approach for the JWST. The most promising option is to provide a very high level of isolation to prevent spacecraft-induced vibrations from propagating into the telescope structure.

The remainder of this paper will discuss the heritage in isolation technology for large space telescopes and particular requirements driving the JWST design. The design and construction of the JWST full spacecraft isolator is then described. A simplified analysis methodology for structures having coupled elastic and viscoelastic constituents is derived. This methodology takes advantage of inherent features in NASTRAN and a viscoelastic material model based upon fractional derivatives. Vibration transmissibility tests performed on each of the beam elements are described and compared to model predictions. Finally, results of modal surveys of the full isolator with a telescope mass and inertia simulator are presented. The trends in frequency and damping of the modal surveys over the temperature range -12 to $+22^\circ$C are compared to the model predictions.

A. Prior Space Telescope Isolators

Prior large space telescopes have employed a single stage of passive isolation at each individual reaction wheel. The isolators on HST function largely attenuate to high-frequency bearing-induced vibrations along each wheel's spin axis.[8] Each isolator consists of six elements with a viscous damping fluid constrained to move between two bellows. A third bellows is provided for thermal expansion of the fluid, as well an outer skirt to prevent fluid escaping in the event of a leak. The springs were tuned to give a 20-Hz axial isolation frequency. Damping in the isolator varies in the range 25–6.25% of critical for temperature in the range -23 to $+43^\circ$C. The transmitted axial force was reduced from 15 N at the worst wheel speed in the hardmount case to 0.11 N with the HST isolators.

The Chandra X-ray Observatory employs a hexapod isolator at each of its six reaction wheels.[9] Each of the six elements in the hexapod is fashioned from compound titanium slotted springs with viscoelastic dampers in parallel with the softer of those two springs. The damper employs two materials to obtain good damping over a wide temperature range, achieving greater than 5% damping over the range -15 to $+54^\circ$C. The isolator resonances at room temperature are at 7 Hz in sway, 10 Hz in bounce, 11 Hz in rocking, and 25 Hz about the spin axis. Urethane bumpers are incorporated in the isolator to limit excursions during launch. This smoothly bilinear spring/bumper system functions as an effective 40-Hz isolator at large amplitude, attenuating the vibration environment during launch for the reaction wheel.

Although not yet flown, the Space Interferometery Mission (SIM) has developed a prototype full spacecraft isolator similar in concept to the one described here for JWST. The SIM isolator consists of three fiberglass beams with constrained layer viscoelastic damping, operating at a 5-Hz isolation frequency.[10] It has been implemented on a full-scale testbed, System Testbed 3 or STB3, having spacecraft bus and optical bench dynamic simulators. The STB3 optical bench is 7 m long, and the bus simulator has a mass of 240 kg. The SIM approach relies on active pathlength control to strongly mitigate vibrations below 10 Hz. The 5-Hz isolation is designed to attenuate vibrations above the control system bandwidth to less than 10 nm.

B. JWST Vibration Isolation Requirements

The core JWST telescope requirements are that diffraction-limited image quality be maintained at a wavelength of 2 μ during science mode and that the stability of the image quality should change by no more than 2% between images taken over a 24-h period.[1] The physical flowdown of these imaging requirements to vibration is a limit of a couple dozen nanometers of wavefront error (WFE), nor more than a few milliarcseconds (mas) of line-of-sight (LOS) pointing error.

WFE is a measure of the aberrations in the light introduced by the optical system. In imaging applications one assumes the light entering the telescope, typically from a distant source such as a star, consists of plane waves. WFE is measured as a spatial rms of the deviation from an ideal wavefront as the light strikes the focal plane. The wavefront error requirement translates into a limit of approximately 10 nm of vibratory piston motions on the PM segments. This figure error is the main source of WFE caused by jitter. Because active wavefront control is performed only sporadically (at intervals of days to weeks), the vibration suppression system is not augmented by active optics.

LOS is a measure of the net lateral image motion on the focal plane, which accounts for rigid-body pointing errors in the telescope, as well as flexible motions within the optical train. LOS is translated into an angular measure in object space by dividing the physical motion of the centroid of light on the focal plane by the telescope's optical lever arm, which is known as the effective focal length. The fine steering mirror attenuates tip and tilt vibrations below 0.4 Hz, thus cancelling most of the rigid-body portion of LOS. The unrejected jitter component of LOS must then be no more than 3–5 mas.

The significant vibratory disturbances that can degrade JWST imaging performance during science mode are the reaction wheels and cryocooler compressor, all located in the spacecraft bus. Mirror positioning actuators, instrument filter wheels, spacecraft mechanisms and thrusters are all coordinated to operate in downtime between imaging. Vibration jitter is calculated for a plausible worst-case condition of two of the six reaction wheels dwelling simultaneously at the worst wheel speed. The compressor drive speed may be adjusted so it does not interact strongly with telescope vibration frequencies. Thus the compressors will consume a small portion of the jitter budget. Figure 2 contains a plot of PM figure error vs wheel speed for cases where the tower is attached rigidly to the bus and also attached through the 1-Hz isolator struts. The analysis was performed using nominal 0.1% damping in the telescope structure and without the first layer of isolation at the reaction wheel. In the hardmount case, figure error vastly exceeds the error allocation at most wheel speeds. Just the single 1-Hz isolation stage is sufficient to bring WFE within or close to the allocated level at the great majority of wheel speeds.

A set of design implementation requirements derives from the small magnitude of the allowed vibration levels. The isolator should be highly linear, so that attenuation occurs for even the smallest of motions. Accelerations at the base of the telescope must be limited to approximately 0.04 μG. The motions of the spacecraft interface to the isolator must be less than approximately 30 nm. These small values limit the range of options in an active system because the noise floor and resolution of sensors and actuators must be approximately an order of magnitude lower than these levels. Sensor issues, together with inherent reliability, motivated the selection of a passive isolation stage between the spacecraft and payload for JWST.

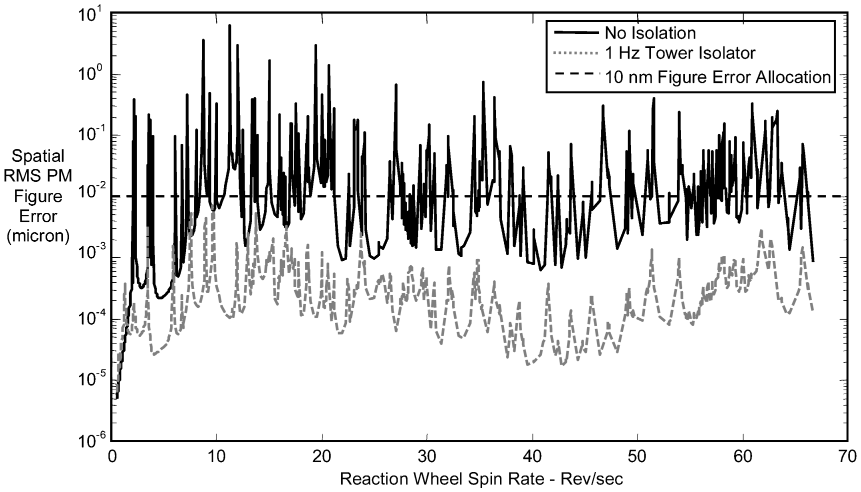

Fig. 2 Primary mirror figure error vs reaction-wheel speed.

The vibration isolator should be stiff enough so that the rigid-body pointing control loop of the spacecraft is not affected. The spacecraft attitude control bandwidth is about 0.02 Hz, so that the isolator rotational modes should be an order of magnitude stiffer than that. A target of 1 Hz was set for the bounce mode of the isolator. Given the large inertias of the telescope and spacecraft, the rotational modes will then be above 0.3 Hz, achieving the goal. Damping in the isolator will also aid in stabilizing the spacecraft pointing control. A requirement for isolator damping has been set at 4% of critical.

A steering mirror provides fine pointing control about the telescope's pitch and yaw axes to an accuracy of a few milliarcseconds. Pointing accuracy about boresight roll is significantly less stringent, on the order of an arcsecond or so, but is uncontrolled by the steering mirror. Pointing control stability of the telescope about the roll axis is based on information from star trackers in the bus and must be translated across the isolator and tower. Thus drifts caused by thermally induced bending in the isolator and tower must be well below an arcsecond over science campaigns lasting one or more days.

Ancillary requirements on the isolator are low weight, compact in envelope with a simple physical interface, sufficient strength to survive launch, reliability, and minimal impact on the telescope cryogenic environment.

II. Isolation Design

Our approach to the JWST isolation problem is to employ dual-stage passive isolation. The first layer of isolation is at the disturbance source. Individual reaction wheels employ the flight-proven Chandra isolator. The cryocooler compressor will be mounted on an isolator similar in design, frequency, and damping to the wheel isolator.

The second stage of isolation is a full isolator placed between the top of the spacecraft bus and the pop-up thermal isolation tower that positions the telescope, as shown in Fig. 3. This isolator further attenuates vibration disturbances from the compressor and six reaction wheels before they propagate into the telescope. The isolator assembly is composed of four graphite/epoxy tubular beams with embedded viscoelastic damping layers, producing a 1-Hz bounce mode with at least 4% damping. The four beams are each clamped at their inner end to the base of the tower. At their outer ends each beam connects to one of the four corners of the bus through a titanium V-flexure that releases axial and bending loads, while transmitting lateral loads through the beam. The result is a soft, near-kinematic support to the tower.

The isolator struts also form part of the thermal control system to the optical payload. The cryogenic payload provides a cold sink at the top of the thermal isolation tower in the vicinity of 50 K. The top panel of the spacecraft bus is thermally controlled near room temperature to provide a constant radiation source. The thin titanium V-flexures decouple the isolator struts thermally from the bus, while the struts are well coupled to the tower. Thus the struts are cold biased. By wrapping the struts in multilayer insulation and providing local heaters with thermostats, they can be controlled to a constant temperature. We chose to control them to 0°C because that represents a peak damping value for the chosen VEM at 1-Hz operating frequency. Because of low conductivity in the tower, the heater power required is small.

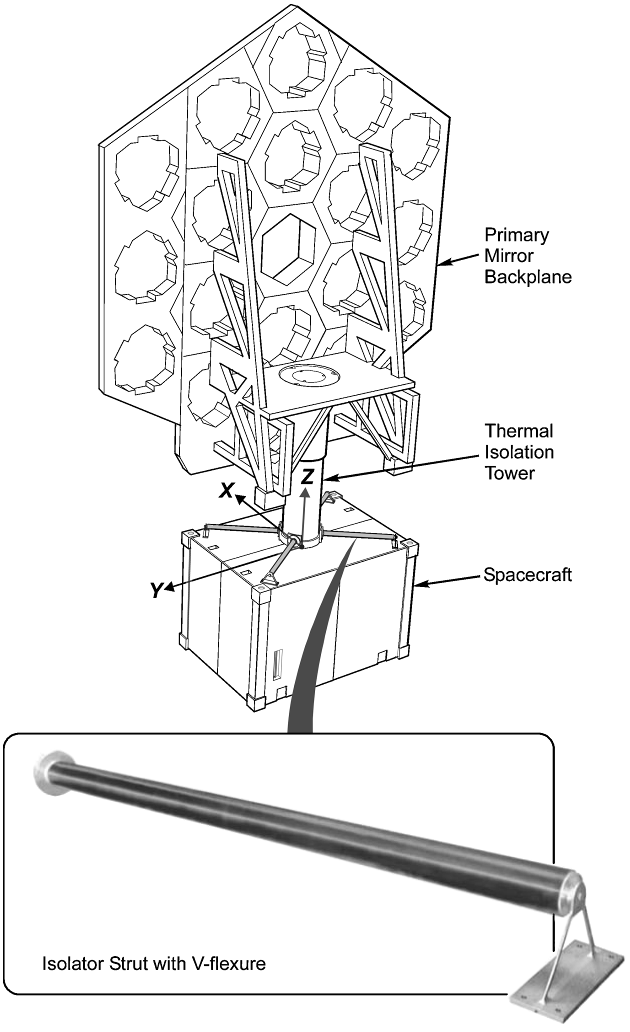

Fig. 3 Spacecraft bus, isolator strut assembly, tower, and PM backplane.

A. Isolator Stiffness

The fixed-pinned lateral stiffness of an individual isolator strut is $k_S = 3EI/L^3$. The vertical and lateral stiffnesses of the isolator assembly can be derived from the beam stiffness as $k_Z = 4\ k_S$ and $k_X = k_Y = 2\ k_S$, respectively. The full stiffness of all four struts acts vertically (in Z), but the effect of the axial flexures is that only two struts carry load in any lateral direction (combinations of Y and Z).

The tower isolator creates a two-body problem, with six rigid-body modes and six isolator modes for the bus-telescope system. The isolator stiffness operates on the reduced mass of this system, which in the bounce Z direction is $m_R = (m_B m_T)/(m_B + m_T)$. For JWST, the reduced mass was approximately 1000 kg for the design when this isolator development took place, corresponding to bus and telescope masses of approximately 2000 kg each. The required isolator strut bending stiffness is a very soft 9860 N/m (56 lb/in.).

The frequencies of the remaining five, nonbounce isolator modes are most easily determined by finite element analysis because of the complex inertias and spatially separated centers of gravity of the bus and telescope payload. It is clear however that maximizing the length of the isolator struts will increase the ratio of isolator rotational frequencies to translational frequencies. For this reason four isolator struts are employed and attached at the outer corners of the bus as shown in Fig. 3. Still, because of the much larger features of the deployed telescope and sunshield relative to the bus size, the isolator rotational modes are roughly one-third the bounce mode frequency.

B. Isolator Construction

Each individual isolator strut is a laminated tubular construction, as depicted schematically in Fig. 4. An inner tube having inner diameter of 2.5 in. carries a static load. It is constructed of low-modulus graphite/epoxy in a layup designed to have low thermal expansion and high strain to failure. A ScotchDamp® viscoelastic damping layer is placed upon the inner tube. Upon this is placed a graphite constraining layer having all 0-deg plies. Because the constraint layer carries no static load as a result of negligible static stiffness in the VEM, thermal expansion is not a concern. Thus the constraining layer can employ high-modulus fiber in a uniaxial layup, which gives the highest specific stiffness. Damping is enhanced by dividing the constraining outer tube into discrete longitudinal segments of length L_c (Ref. 11). This causes a portion of the axial load from the inner tube to weave in and out of the outer tube segments by transferring load in shear through the VEM.

To gain insight into behavior as segment length and constraining layer stiffness vary, the construction of each of the four prototype struts was different. Struts 1 and 2 have segment length $L_c = 10.5$ in., and struts 3 and 4 have $L_c = 8.75$ in. The optimum segment length for peak damping at 1 Hz and 0°C for this construction is around 9 in. The number of plies in the constraining layer is three for struts 1 and 3 and four for struts 2 and 4. End fittings and the V-flexure complete the $L = 42$ in. strut, as shown in the photograph in Fig. 3. The end flexure is designed so that its compliance along the axial direction of the strut is more than a factor of 10 less than the lateral bending stiffness of an isolator strut. By this means, the isolation performance is dominated by transmission in lateral bending through the beams.

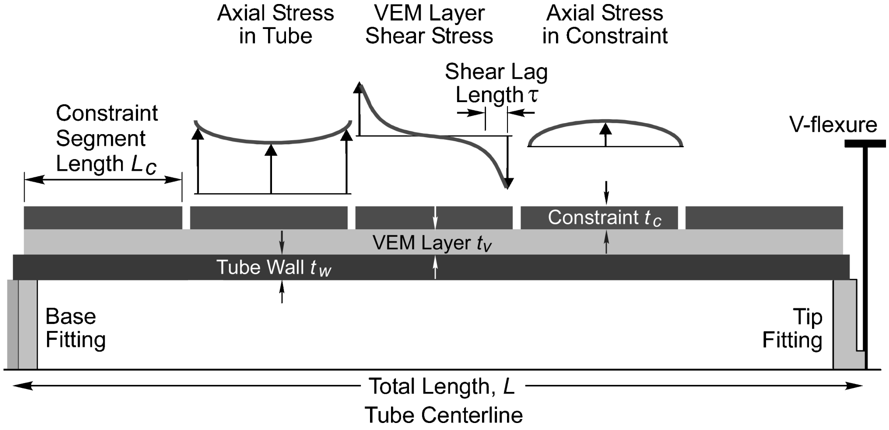

Fig. 4 Details of isolator strut construction.

III. Analysis Methodology for Structures with a Viscoelastic Constituent

As opposed to a typical elastic structure, in which properties remain quite constant, the stiffness and damping properties of a viscoelastic structure vary greatly with both temperature and frequency. It turns out, in fact, that peak damping is achieved at a point in temperature-frequency space, where the stiffness properties of the VEM are changing the fastest. This fact makes designing a damping treatment and achieving the correct stiffness balance between elastic and lossy portions of the structure inherently difficult. The analysis is also difficult because standard finite element codes operate most efficiently with constant material properties. In the course of this research, an efficient means was devised for analyzing structures with viscoelastic constituents. The method employs a finite element code such as NASTRAN to generate a set of real normal mode shapes, frequencies, and modal damping matrix for a nominal operating temperature and frequency. This data set serves as the basis for a frequency-domain analysis in which properties are adjusted for the actual operating temperature and response frequency. This postprocessing of finite element results has been undertaken in a MATLAB® environment.

The following development is conducted using a single material property to characterize the lossy portions of the structure. In this case shear modulus in the viscoelastic material is used because constrained layer implementations exercise the VEM only in shear. If more than one type of damping treatment is employed in a structure, multiple structural partitions would be required, which is a straightforward extension of the methodology presented here.

A. Fractional Derivative Viscoelastic Material Model

The analysis begins by defining the complex VEM shear modulus G^* vs operational frequency Ω and absolute temperature T (Ref. 12):

$$G^*(\Omega, T) = G(\Omega, T)[1 + j\eta(\Omega, T)] \tag{1}$$

The complex shear modulus is partitioned in terms of storage modulus, $G = \mathrm{Re}(G^*)$, and loss factor, $\eta = \mathrm{Im}(G^*)/\mathrm{Re}(G^*)$, also called the loss tangent. Most VEMs are thermorheologically simple materials. This trait allows a family of complex modulus curves for varying temperatures T and frequencies $f = \Omega/2\pi$ to be described by a single curve. To do this, a functional relation between T and f, known as the reduced frequency, is defined:

$$f_R(f, T) = f\alpha(T) \tag{2}$$

The temperature shift function $\alpha(T)$ is evaluated at the operating temperature and used to scale the frequency of vibration. It is known

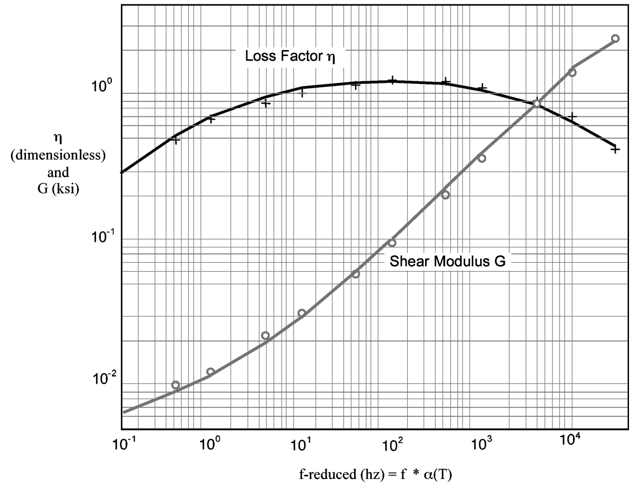

Fig. 5 Measured VEM storage modulus (○) and loss factor (+) as a function of reduced frequency: ——, fractional derivative fit to data.

that the VEM softens as either frequency is lowered or temperature is raised. Thus, at higher temperatures the shift function decreases to produce a lower apparent (reduced) frequency. Conversely, when it is cold the VEM is firmer, and apparent frequency must be increased. The shift function is derived from testing at a variety of temperatures and frequencies. The Arhennius form is often used to define the shift function, that is, the log of the shift function is modeled as linear in the inverse of the absolute temperature.[13] In this work a quadratic Arhennius form was found to give a slightly better fit to measured VEM behavior:

$$\log_{10}[\alpha(T)] = \alpha_0 + \alpha_1/T + \alpha_2\big/T^2 \tag{3}$$

The complex shear modulus and loss factor properties are fit quite effectively in the frequency domain using a simple four-parameter fractional derivative model.[14] The form of the model is

$$G'(f_R) = G_0\frac{1+(jf_R/a)^\beta}{1+(jf_R/b)^\beta} \tag{4}$$

where G_0 is the low-frequency asymptotic stiffness and β is related to the slope of the modulus curve. β is typically in the vicinity of $\frac{1}{2}$ and represents a fraction of a whole derivative; in other words, behavior is about halfway between elastic (no time dependence) and viscous (single derivative with time). Notice that at very low ($f_R \ll a$) and very high ($f_R \gg b$) frequencies, G' is essentially real. G' has its most imaginary contribution for $a < f_R < b$, giving the highest level of damping where modulus is changing most rapidly with frequency (and hence with temperature). A plot of the storage and loss modulus from a fractional derivative model of the ScotchDamp material employed in the isolator's damping layer is shown in Fig. 5. This material has an exponent of approximately $\beta = 0.6$.

To simplify notation in the ensuing sections, the complex modulus will be recast in terms of frequency in the Fourier domain Ω:

$$G^*(\Omega, T) = G_0\frac{1+a'(T)(j\Omega)^\beta}{1+b'(T)(j\Omega)^\beta} \tag{5}$$

where $a'(T) = [\alpha(T)/2\pi a]^\beta$ and $b'(T) = [\alpha(T)/2\pi b]^\beta$.

B. Frequency-Domain Solution of Frequency and Temperature-Dependent Dynamics Equations

The derivation of the system dynamical equations will be conducted in the frequency domain because that is the desired solution form for evaluation of isolator performance. Bagley[15] has shown that dynamical equations formulated in the frequency domain using a fractional derivative material model transform into real, causal solutions in the time domain. The equations of motion in discrete displacement coordinates of the finite element model u are

$$[(j\Omega)^2 M + \tilde{K}(\Omega, T)]\{u(\Omega)\} = \{\boldsymbol{F}(\Omega)\} \tag{6}$$

where $\tilde{K}$ is a complex, frequency- and temperature-dependent stiffness matrix.

Finding an eigenvalue solution to the left-hand side of Eq. (6) is possible, but computationally prohibitive for even moderately sized systems. The approach outlined in Ref. 14 requires generation and solution of a set of first-order equations that expand in multiples of the least common denominator of β and 2 up to the highest derivative in the system, $2+\beta$. For instance, if β were simply $\frac{1}{2}$, then fractional derivatives of order 0, $\frac{1}{2}$, 1, $1\frac{1}{2}$, 2, and $2\frac{1}{2}$ would be required, that is, a complex eigenvalue problem of five times the original size is required. For the case studied here, where $\beta = 0.6$, the lowest common denominator with 2.6 is 0.2, and the problem dimensionality would be multiplied by 14. Alternatively, one could solve Eq. (6) directly in the frequency domain. For very large systems, that can also be computationally expensive because a large, complex matrix must be inverted at every frequency evaluated. The approach adopted in this research is to use a set of real normal modes to reduce the basis of the problem and then perform a direct inversion in the reduced modal space.

1. Nominal Real Eigenvalue Problem Used as Basis for Solution

One can think of the system structural model as being divided into elastic and lossy regions. For simplicity, we will consider that all of the lossy regions employ the same viscoelastic material, so that their properties scale identically with frequency and temperature. As such, the system stiffness matrix can be thought of as the sum of elastic and lossy parts K_E and K_V, respectively. The system stiffness matrix K is the sum of all real element stiffness matrices, elastic or lossy. It is used in the solution of the system eigenvalue problem. The structural damping matrix $K4$ is computed by summing the elemental stiffness matrices scaled by their material loss factors. Having these two matrices allows us to discriminate between elastic and lossy parts. Material properties in the lossy region are computed for a nominal operating temperature T_0 and frequency Ω_0, resulting in nominal dynamic stiffness and loss scaling factors S_0^V and η_0^V, respectively,

$$K \equiv K_E + S_0^V K_V \tag{7a}$$

$$K4 \equiv \eta_0^V S_0^V K_V \tag{7b}$$

Following construction of the system matrices in NASTRAN, the real eigenvalue problem $K\boldsymbol{\Phi} = M\boldsymbol{\Phi}\omega^2$ is solved to produce a matrix of real normal mode shapes $\boldsymbol{\Phi}$ and a diagonal matrix of natural frequencies squared ω^2. This represents the solution to the homogeneous equations of motion with all damping terms ignored, $M\ddot{u} + Ku = 0$. Physical displacement is expanded in terms of the mode shapes $u = \boldsymbol{\Phi}h$. The physical stiffness and loss matrices are then transformed from physical coordinates $\boldsymbol{u}$ to modal coordinates $\boldsymbol{h}$:

$$\boldsymbol{\Phi}^T K\boldsymbol{\Phi} \equiv \boldsymbol{\Phi}^T\big[K_E + S_0^V K_V\big]\boldsymbol{\Phi} = \omega^2 \tag{8a}$$

$$\boldsymbol{\Phi}^T K4\boldsymbol{\Phi} \equiv \boldsymbol{\Phi}^T\big[\eta_0^V S_0^V K_V\big]\boldsymbol{\Phi} = \kappa 4 \tag{8b}$$

The eigenvectors have been normalized to produce an identity modal mass matrix. Notice that the modal loss matrix $\kappa 4$ is not diagonalized, indicating coupling between modes because of the damping terms. The matrices $\boldsymbol{\Phi}$, ω^2, and $\kappa 4$ describe the dynamic properties of the system for the assumed nominal stiffness and loss factor properties.

A truncated set of modes can sometimes be used with a small loss of accuracy if the excitation frequency is below the frequency of the highest included mode. For instance, in the two-stage isolation case the JWST reaction-wheel jitter analyses for wheel speeds up to 80 rev/s produce very similar results whether modes through 100 or 300 Hz are included. This is because of the dual roll-off effect of both isolators on high-frequency response. Thus, in addition to reduced transmission of high-frequency harmonics of wheel speed, an additional advantage of the two-stage isolator approach is reduced sensitivity to modeling accuracy and analysis errors.

2. *Solution in Modal Subspace*

The second analysis phase scales the nominal properties used to generate the real normal modes to represent actual properties as a function of true operating temperature and frequency. This step was performed using MATLAB in the study described here. Equation (6) is transformed from discrete to modal coordinates to obtain

$$[(j\Omega)^2 I + \tilde{\omega}^2(\Omega, T)]\{\boldsymbol{h}(\Omega)\} = [\boldsymbol{\Phi}]^T \boldsymbol{F}(\Omega) \tag{9}$$

where $\tilde{\omega}^2(\Omega, T) = \boldsymbol{\Phi}^T \tilde{K}(\Omega, T)\boldsymbol{\Phi}$ is a full generalized stiffness matrix. Being complex, this matrix will capture both the stiffness and loss characteristics of the system. In terms of the matrices generated in the finite element code, the generalized stiffness matrix assumes the form

$$\begin{aligned}\tilde{\omega}^2(\Omega, T) = {} & [\boldsymbol{\Phi}]^T[(1 + i\eta_E)K_E \\ & + S^V(\Omega, T)(1 + i\eta^V(\Omega, T))K_V][\boldsymbol{\Phi}]\end{aligned} \tag{10}$$

A constant loss factor term η_E has been included for the elastic portion of the structure. This loss factor is typically much lower than that of the lossy portion. A value of $\eta_E = 0.01$ ($\frac{1}{2}$% damping) was used to model the tests described in this paper. $S^V(\Omega, T)$ and $\eta^V(\Omega, T)$ are real-valued dynamic stiffness and loss scale factors evaluated at the operating conditions. To continue, one needs to know the matrices $\boldsymbol{\Phi}^T K_E \boldsymbol{\Phi}$ and $\boldsymbol{\Phi}^T K_V \boldsymbol{\Phi}$ separately. These can be obtained from Eqs. (8a) and (8b):

$$\boldsymbol{\Phi}^T K_E \boldsymbol{\Phi} = \omega^2 - \kappa 4 \Big/ \eta_0^V \tag{11a}$$

$$\boldsymbol{\Phi}^T K_V \boldsymbol{\Phi} = \kappa 4 \Big/ \left(\eta_0^V S_0^V\right) \tag{11b}$$

Finally, one obtains the following relation for complex generalized stiffness in terms of known quantities:

$$\tilde{\omega}^2(\Omega, T) = (1 + i\eta_E)\left[\omega^2 - \frac{\kappa 4}{\eta_0^V}\right] + \frac{S^V(\Omega, T)[1 + i\eta^V(\Omega, T)]}{\eta_0^V S_0^V}\kappa 4 \tag{12}$$

This expression is evaluated at every frequency of interest and substituted in Eq. (9), allowing solution first for the modal coordinates

$$\boldsymbol{h}(\Omega, T) = [\tilde{\omega}^2(\Omega, T) - \Omega^2 I]^{-1}\boldsymbol{\Phi}^T \boldsymbol{F}(\Omega) \tag{13}$$

and then physical response can be recovered using $\boldsymbol{u} = \boldsymbol{\Phi h}$.

The approximation inherent in this analysis is that the mode shapes computed for the nominal stiffness properties S_0^V and ignoring damping provide a sufficient basis for the mode shapes of the system evaluated using the operating properties $S^V(\Omega, T)$ and $\eta^V(\Omega, T)$. The use of a basis of real normal modes speeds the analysis significantly, is straightforward to code by taking advantage of standard finite element solvers, and has been found to give reasonable results for the class of problem described in this paper.

C. Incorporation of Constrained Layer Damping Theory

One can compute the stiffness enhancement and damping introduced by a segmented constraining layer using a simple closed-form solution that originated in bonded joint theory.[16] The analysis presented here follows the three-layer derivation for damped beams in Ref. 17. One starts by defining the stiffness per unit width of the three layers in the damped tube or member: wall axial stiffness $k_W = E_W t_W$; constraint-layer axial stiffness $k_C = E_C t_C$; and viscoelastic layer shear stiffness $k_V(\Omega, T) = G_V^*(\Omega, T)t_V$. The wall and constraint properties are assumed real, having trivial damping compared to the VEM, and the VEM property is complex, as discussed earlier. The decay length, the distance to transfer load from inner tube to constraining layer, is

$$\lambda = \sqrt{\frac{k_W k_C}{k_V(k_W + k_C)}} \tag{14}$$

A complex length is obtained, but this is not of concern as nothing is being measured. It was shown in Ref. 11 that the segmentation length for maximum damping is $L_C \cong 3.28|\lambda|$. Complex stiffness per unit width of the net tube is given by

$$\begin{aligned}\tilde{k}(\Omega, T) &= \frac{k_W + k_C}{1 + (k_C/k_W)[\tanh(L_C/2\lambda)/(L_C/2\lambda)]} \\ &\equiv S^V(1 + i\eta^V)k_W\end{aligned} \tag{15}$$

This enhanced stiffness function $\tilde{k}(\Omega, T)$ determines the dynamic stiffness scaling factor $S^V(\Omega, T) = |\tilde{k}/k_W|$, and the loss factor scaling factor $\eta^V(\Omega, T) = \mathrm{Im}(\tilde{k})/\mathrm{Re}(\tilde{k})$, which are employed in Eq. (12). They are also evaluated at a nominal temperature and frequency to determine the nominal properties used in the baseline NASTRAN analysis. For the JWST segmented constraint isolator beams, the axial modulus of the underlying beam is inflated by a nominal factor $S_0^V = 1.15$. This accounts for stiffness added to the underlying tube by the dynamic stiffness in the constraining layer. A nominal loss factor $\eta_0^V = 0.1$ (5% damping) for such a damped beam is also employed.

The methodology described here allows finite element results generated for a constant set of properties to be postprocessed using a fractional derivative material model and analytic solutions for the effects of added damping treatments. A segmented constraining layer was employed here. One could imagine the use of other damping treatments having closed-form solutions, such as the Ross–Kerwin–Ungar equations used for layered damping treatments.[18] Or one could forego including analytic solutions for damping treatments and simply model the viscoelastic medium using discrete finite elements.

IV. Unit Strut Tests

Before testing the full isolator system, unit frequency and damping free decay (twang) tests were performed on each strut at room temperature to validate the model. Transmissibility tests were performed on strut 2 at several temperatures using the setup shown in Fig. 6.

Because of height and mass limitations in the laboratory, strut 2 was mass loaded to produce a 2-Hz lateral mode. This was achieved using a 147-lb tip mass suspended by an 82-in.-long, high-strength cord, having a 0.4-Hz pendulum frequency. The steel mass was fashioned as a square frame so that, when attached to the V-flexure, its center of mass coincided with the strut tip. The mass could then be shaken laterally without inducing rotation. Strut 2 is shown wrapped in multilayer insulation. Temperature was controlled by pumping chilled fluid through Tygon™ tubing wrapped spirally around the strut.

A. Twang Test Results

Table 1 contains frequency and damping data and model predictions for the four struts with no tip mass at room temperature and for strut 2 with the 147-lb/tip mass at 7°C. At the first mode frequencies in those configurations, 22 and 7°C were close to the optimum temperatures for peak damping. For the heavily loaded case, the frequency correlation between model and test was the best, perhaps because the mass distribution was better known than for the non-mass-loaded case. Damping predictions came out very close to measurements for all except strut 1, which achieved damping at 89% of the predicted value. For struts 2–4 the average modal damping prediction was within 95% of the predicted value. Following fabrication of strut 1, manufacturing process improvements had been made, which explains the better correspondence between test and analysis for struts 2–4. The thicker constraining layer in struts 2 and 4 gave an extra 1% damping as compared to struts 1 and 3. It did not increase frequency because the extra constraint ply adds mass as well as stiffness. The effect of the longer constraining layer segment length of struts 1 and 2 was to increase frequency when compared to struts 3 and 4, as expected, whereas there was an inconclusive effect on damping. That indicates that the optimum segment length is between 8.75 and 10.5 in., as the analysis predicts.

B. Transmissibility Test Results

Transmissibility was measured by exciting the large tip mass in the lateral direction, measuring the applied force as well as the

Table 1 Twang test-model correlation

Strut	L_c, in.	No. plies	Temp, °C	Tip mass, lb	Mode	Frequency, Hz		Damping, %	
						Measured	Analytic	Measured	Analytic
1	10.5	3	22	0	1	30.3	33.4	5.25	5.91
2	10.5	4				29.5	32.6	6.43	6.85
3	8.75	3				28.9	32.4	5.40	5.48
4	8.75	4				28.9	31.6	6.27	6.13
2	10.5	4	7	147	1	1.96	1.98	5.71	5.76
					2	160	167	3.86	3.92
					3	461	464	3.01	2.54

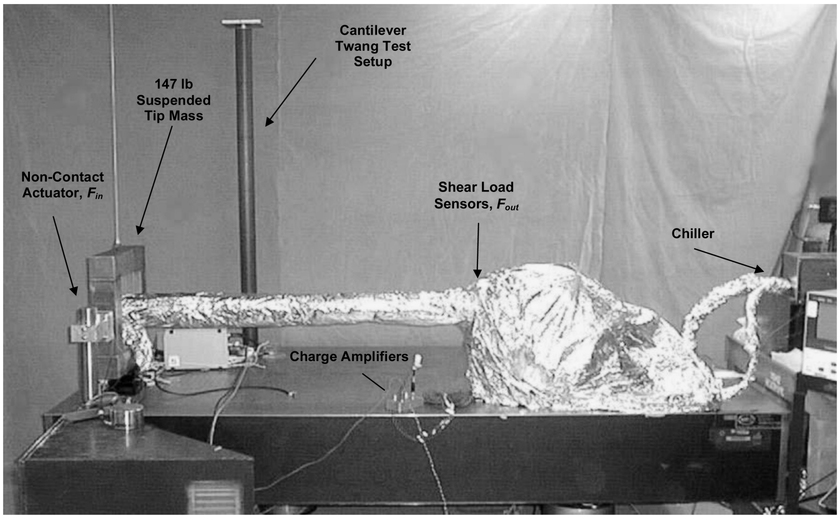

Fig. 6 Unit transmissibility and twang test setups.

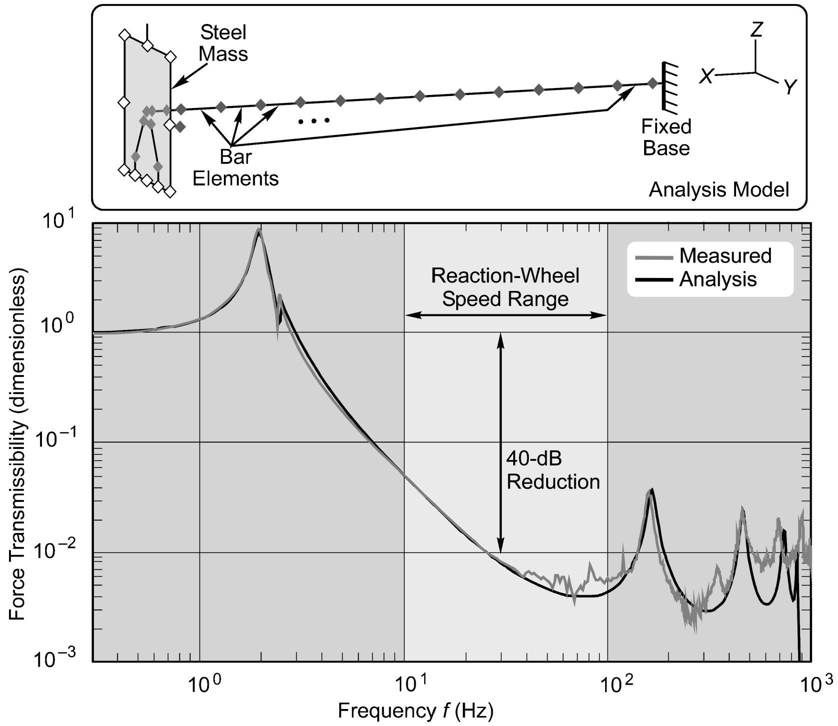

Fig. 7 Unit transmissibility comparison between measurement and test at 7°C.

reaction shear force at the base of the beam. To minimize sneak load paths, a noncontact actuator was fabricated from a neodymium-iron-boron magnet affixed to the test mass and a coil affixed to ground. The magnet was mounted on a quartz load cell with custom charge amplifier, providing the input force signal F_{in}. The output force was monitored using three load cells supporting the base of the strut. The shear force outputs were combined into a single charge amplifier, producing the net shear load in the isolator strut F_{out}. The transfer function $F_{\text{out}}/F_{\text{in}}$ provides the measure of transmissibility. Tests were performed at several temperatures between 1.6 and 27.5°C. At the first mode frequency in this configuration, roughly 2 Hz, the optimum damping temperature was found to be 7°C. The 5.7% damping measured for the first mode in the heavily loaded configuration would be considered excellent for a constrained layer approach.

Figure 7 shows the correspondence between measured and analytic vibration transmissibility. The vibration attenuation is greater than 40 dB through most of the wheel speed range planned for JWST. The high-frequency resonances were well damped, so that in no case was high-frequency vibration attenuation less than 28 dB. The first cantilever bending mode near 2 Hz and the two local bending modes near 160 and 460 Hz all had good correspondence with frequency and amplitude. The third and higher local bending modes started to diverge from the prediction. Because the graphite tube was modeled with only 12 bar elements, the third local bending mode would have only about four elements per half-wavelength. Axial transmissibility was not measured, but we feel this should be lower than lateral transmissibility because the V-flexure makes axial stiffness significantly lower than lateral stiffness of the beam.

An issue that often arises with very soft isolators is whether extraneous hardware such as electrical cabling will conduct alternate load paths around the isolator. This issue was addressed through a test. The number and size of wires between the JWST payload and the spacecraft is estimated at 2000 wires. Because this will be distributed across the four struts, a representative harness with 500 wires of various gauge was draped along the isolator strut, connecting the tip mass and the base. Transmissibility measurements were taken and compared to those taken on a clean isolator. Transmissibility did not increase appreciably at any frequency, and, in fact, some of the high-frequency peaks were significantly attenuated because of added damping from the harness.

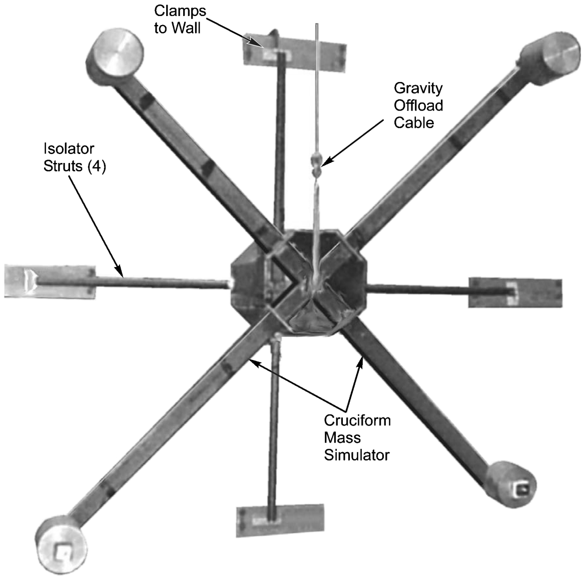

Fig. 8 Full-scale, five-degree-of-freedom isolator test setup.

V. Full-Scale Modal Test

The validation approach was to address transmissibility at the unit level through high-frequency tests that could be matched more easily to models. The ability to produce a true 1-Hz isolator at operating temperature was verified by a full-scale modal test with temperature control. Figure 8 shows the test setup to achieve this. The mass simulator took the form of a large cruciform, 4.48 m across in X and 3.72 m across in Y, its four steel arms each supporting a 170-kg tip weight. The lengths were chosen to match the inertia of the deployed JWST telescope. The total 1022-kg mass replicates the reduced mass of the bus-telescope system. The simulator was supported on a 28-ft steel cable in a high bay, giving a 0.17-Hz pendulum frequency. The four isolator struts were bolted at their base to the mass simulator's central structure, and the V-flexures were clamped to a wall. The support cable was placed on a pivot at the exact mass center of the simulator. Thus, five rigid-body degrees of freedom were available, all except vertical translation. The struts were chilled as described for the unit tests. Modal surveys were performed to extract fundamental isolator mode frequencies using both hammer and shaker excitations. The shaker results were cleaner because more kinetic energy could be forced into the massive test article. Tests were performed from room temperature down to -12°C.

A summary of the modal survey results for a representative set of three of the five suspension modes is shown in Fig. 9. These modes are lateral sway T_2, bounce T_Z, and rocking about X (R_X). The other two modes, rocking about Y (R_y) and torsion (R_z) are left off to simplify the plots, but follow the same trends. The solid lines in Fig. 9 show analytic predictions, and the symbols show measurements. One can see for the bounce mode that damping has a peak of 5.0% at 0°C, and that frequency is 0.984 Hz at that temperature. Thus the frequency and damping goals for the isolator are met. As temperature is lowered, the modal frequencies increase, but less so in the measurements than in the analysis. Damping peaks in all of the modes near 0°C, with less damping at warmer and cooler temperatures. One is ensured of at least 4% damping in the range ±5°C. Analysis predicts about 1% (absolute) more damping than was measured. Test-analysis correlation is not as close as for the unit tests. One factor is that the four struts were all different, whereas averaged strut properties were used for the system analysis to keep the software simple. Strut 1, being built before the process improvement, was not as effective as struts 2–4. Modeling detail on the mass

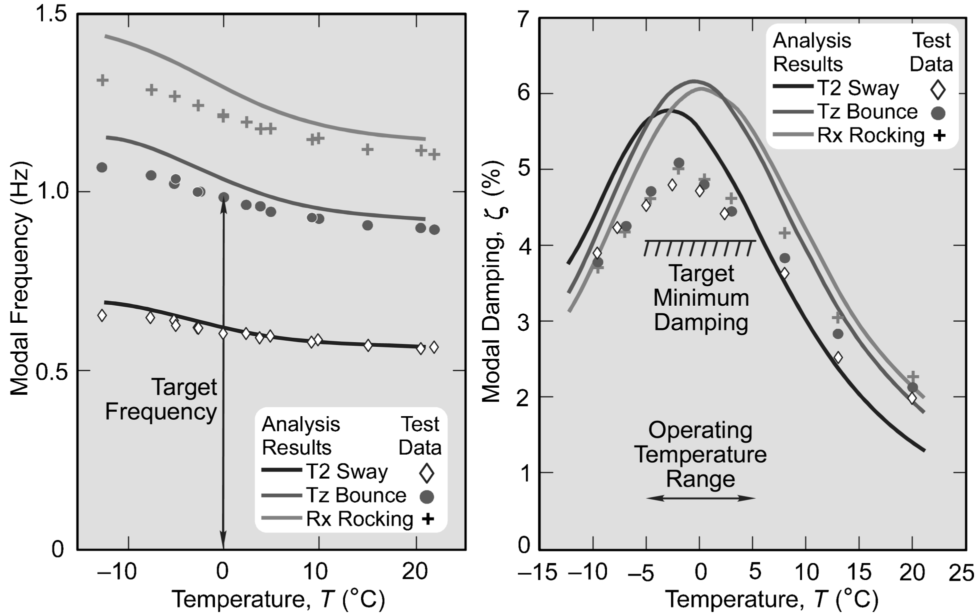

Fig. 9 Modal frequency and damping for five-degree-of-freedom test: analysis (lines) vs measurements (symbols).

simulator is not great, and there is some bending flexibility in the plates on the mass simulator central structure to which the struts are bolted. If strain energy were diverted into this interface plate from the struts, that would explain to some extent why measured damping is lower than analysis, and why the stiffness increase with cold is more muted in the hardware than in the analysis. Given these caveats, we feel the frequency- and temperature-dependence trends displayed in the model are substantially predictive of the measured performance.

VI. Conclusions

This research program has successfully developed a prototype 1-Hz full spacecraft isolator, the largest built to this time. It meets all requirements, including stiffness, weight, strength, damping, thermal distortion, and simplicity. The full spacecraft isolator succeeds in attenuating response to multiple vibration sources inside the spacecraft bus.

An analysis technique that fits into the standard modeling framework for large space observatories by taking advantage of existing finite element tools was developed. By scaling a set of mode shapes for nominal properties, performance at numerous frequencies and an arbitrary operating temperature can be computed without rerunning the system eigenvalue problem. Using a fractional derivative viscoelastic material model, the time-consuming and error-prone job of looking up VEM stiffness and loss factor on a reduced frequency nomogram was eliminated. The modeling capability predicted hardware damping performance to an accuracy of 5% in unit tests. In the more complex full-scale test the modeling technique was shown capable of predicting the temperature that gives peak damping and trends in damping and stiffness vs temperature and frequency.

Transmissibility tests have shown individual isolator elements effective up to a kiloHertz. The damped beams act in some sense as wave absorbers to high-frequency vibrations. Because the integrated model of the JWST observatory predicts acceptable jitter performance if the isolator meets its specifications and because the testing confirms the ability to both build the isolator and to analyze it, we can now predict with confidence that JWST will have excellent on-orbit dynamic performance.

The beam isolator concept can be implemented with either three or four struts. Four were chosen for JWST to fit the top deck of the spacecraft. This configuration has three major advantages over the competing six-strut hexapod arrangement of axial isolator struts. The beam isolator packages more compactly and weighs significantly less. Also, the hexapod struts can transmit loads transverse to their axis, whereas the beam isolator struts are flexured to minimize transmission of loads in other than the intended lateral direction. The vibration isolator is the first stage in thermal management of the telescope. The isolator will be controlled to 0°C within about 1°C using thermostat-controlled heaters, although a looser range of ±5°C is tolerable. This will present the thermal isolation tower with a very stable interface, eliminating conduction as a source of thermal instability in the telescope.

Acknowledgment

This effort was wholly funded by a Northrop Grumman Space Technology internal research and development program before the award of the JWST full-scale development contract.

References

[1] Nella, J., Atcheson, P., Atkinson, C., Au, D., Bronowicki, A., Bujanda, E., Burt, J., Cohen, A., Davies, D., Lightsey, P., Lynch, R., Lundquist, R., Mohan, M., Pohner, J., Reynolds, P., Rivera, H., Texter, S., Shuckstes, D., Simmons, D., Smith, B., Sullivan, P., Waldie, D., and Woods, R., "JWST Observatory Architecture and Performance," *Optical, Infrared, and Millimeter Space Telescopes, Proceedings of SPIE*, Vol. 5487, edited by J. C. Mather, 2004, pp. 576–587.

[2] Bely, P.-Y. (ed.), *The Design of Large Optical Telescopes*, Springer-Verlag, New York, 2002, Chap. 7.

[3] Blair, M. A., "HST Modal Survey Test Report," Lockheed, Rept. EM SET 212, Aug. 1986.

[4] White, C. V., and Levine, M. B., "Experiments to Measure Material Damping and Stiffness at Cold Temperatures," Jet Propulsion Lab., Document D-22047, Pasadena, CA, 2002.

[5] Goldie, J. H., "Eddy Current-Based Vibration Damping for Aerospace Structures," *Damping '91*, edited by L. Rogers, Wright–Patterson AFB, Rept. WL-TR-91-3078, Paper FDA, Akron, OH, Aug. 1991.

[6] Neat, G. W., Melody, J. W., and Lurie, B. J., "Vibration Attenuation Approach for Spaceborne Optical Interferometers," *IEEE Transactions on Control Systems Technology*, Vol. 6, No. 6, 1998, pp. 689–700.

[7] Masterson, R. A., and Bronowicki, A. J., "Simplified Teldix RDR 68-4 RWA and Isolator Models," TRW, IOC M740-61, March 2000.

[8] Davis, L. P., Wilson, J. F., and Jewell, R. E., "Hubble Space Telescope Reaction Wheel Assembly Vibration Isolation System," *Structural Dynamics and Control Interaction of Flexible Structures*, NASA Rept. N87-22702, March 1986, pp. 669–690.

[9] Nye, T. W., Bronowicki, A. J., Manning, R. A., and Simonian, S. S., "Applications of Robust Damping Treatments to Advanced Spacecraft Structures," *Advances in the Astronautical Sciences*, Vol. 92, Feb. 1996, pp. 531–543.

[10] Bronowicki, A., MacDonald, R., Gursel, Y., Goullioud, R., Neville, T., and Platus, D., "Dual-Stage Vibration Isolation for Optical Interferometer Missions," *Interferometry in Space, Proceedings of SPIE*, Vol. 4852, 2002, pp. 753–763.

[11] Plunkett, R., and Lee, C. T., "Length Optimization for Constrained Viscoelastic Layer Damping," *Journal of the Acoustical Society of America*, Vol. 48, No. 1, 1970, pp. 150–161.

[12] Nashif, A. D., Jones, D. I. G., and Henderson, J. P., *Vibration Damping*, Wiley, New York, 1985, Chap. 7.

[13] Morganthaler, D. R., "Practical Design and Analysis of Systems with Fractional Derivative Materials and Active Controls," *Damping '91*, Paper BCA, 1991.

[14] Bagley, R. L., and Torvik, P. J., "Fractional Calculus—A Different Approach to the Analysis of Viscoelastically Damped Structures," *AIAA Journal*, Vol. 21, No. 5, 1983, pp. 741–748.

[15] Bagley, R. L., "Applications of Generalized Derivatives to Viscoelasticity," Air Force Materials Lab., TR-79-4103, Akron, OH, Nov. 1979.

[16] Segerlind, J. L., "On the Shear Stress in Bonded Joints," *Journal of Applied Mechanics*, Vol. 35, March 1968, pp. 177, 178.

[17] Kress, G., "Improving Single Constrained-Layer Damping Treatment by Sectioning the Constraining Layer," *The Role of Damping in Vibration and Noise Control*, Design Engineering Div. Vol. 5, American Society of Mechanical Engineers, New York, 1987, pp. 41–48.

[18] Ross, D., Ungar, E., and Kerwin, E., "Damping of Plate Flexural Vibrations by Means of Viscoelastic Laminate," *Structural Damping*, edited by J. Ruzicka, American Society of Mechanical Engineers, New York, 1959, pp. 49–88.

G. Agnes
Associate Editor